Sensors & Actuators: A. Physical 343 (2022) 113661

Contents lists available at ScienceDirect

Sensors and Actuators: A. Physical

journal homepage: www.journals.elsevier.com/sensors-and-actuators-a-physical

Modelling analysis for design of microshutters with new electrode configuration

Ming Ke [a,b,*], Alexander S. Kutyrev [a,c], Carl A. Kotecki [a], Kyowon Kim [a,d], Matthew A. Greenhouse [a], Meng-Ping Chang [a], Rainer Fettig [a,e], Regis P. Brekosky [a], Yongjie Hu [b]

[a] NASA Goddard Space Flight Center, Greenbelt, MD, USA
[b] University of California, Los Angeles, Los Angeles, CA, USA
[c] University of Maryland, College Park, MD, USA
[d] Science Systems and Applications Inc., Lanham, MD, USA
[e] Beacon System Inc., Coral Springs, FL, USA

ARTICLE INFO

Keywords:
Electrostatic
Actuator
Microshutter array
Multi-object spectroscopy

ABSTRACT

The Next Generation Microshutter Array (NGMSA) is an all-electrostatic actuated, programmable light transmission device used for multi-object spectroscopy. The latest NGMSA is designed to operate by applying a voltage difference between the shutter blade electrode and a single back wall electrode. We investigate the effects of different wall electrode configurations and present a bi-electrode design that allows reliable shutter actuation at a voltage difference of 70V.

1. Introduction

A microshutter array (MSA) is a programmable 2D field mask device that consists of a two-dimensional array of selectively controllable shutters that enables multi-object spectroscopy in the target field of view of a telescope. The shutters block out the light of overlapping spectrums from multiples sources that would be visible when observed by a telescope with a large field of view. Space-based spectroscopy is time consuming and expensive. Multi-object spectroscopy is a game changing technology that multiplies the science return for a given telescope observation time period. While it is easy to make custom masks for each science objective, a remotely reconfigurable mask is necessary in space.

The first generation MSA design was chosen for the Near Infrared Spectrograph (NIRSpec) instrument installed on the James Webb Space Telescope (JWST) to simultaneously acquire optical spectrum from hundreds of celestial targets [1]. Various microshutter technologies have been developed since the 1990′s. Examples include roll-blind type shutters [2], comb drive shutters [3], and parallel motion shutters [4,5]. Roll-blind type shutters use layers of material with varying thermal expansion coefficients. Heating the blinds will cause them to roll up and open. Closing is typically done electrostatically. Response time of these shutters tends to be slower, and relatively large voltages are required for closing. Electrostatically modulated comb drives and parallel motion shutters are also shutter designs that have been used in optical imaging applications. These devices can achieve high switching speed at lower voltages (around 70V) but suffer from low fill factors. In contrast, magnetically and electrostatically actuated rotational shutters [6–10], including MSAs, are most spatially compact, have the highest fill factor out of all microshutter designs, and can be designed to have a short response time.

The first generation MSA installed on NIRSpec utilizes a magnetic actuation and electrostatic latching operation scheme [11–13]. The bulky magnet assembly adds complexity to the system. The Next Generation Microshutter Array (NGMSA) is an effort to develop MSAs with all-electrostatic operation to remove the magnet mechanisms completely. The feasibility of NGMSA has been successfully demonstrated for space flight on the Far-ultraviolet Off Rowland-Circle for Imaging and Spectroscopy (FORTIS) sounding rocket mission in 2019 [9].

The current NGMSA unit shutter design used in the FORTIS mission is shown in Fig. 1(b). A rectangular shutter blade is mounted on a silicon (Si) frame by the two ends of a torsion bar. One electrode is located on top of the shutter blades. A vertical wall electrode is located on the back wall of a Si frame, separated by an electrically insulated layer. Devices with this design utilized a dynamic actuation scheme. A short, high voltage pulse is applied to the shutter electrode to set the blade in

* Corresponding author at: NASA Goddard Space Flight Center, Greenbelt, MD, USA.
E-mail address: ming.ke@nasa.gov (M. Ke).

https://doi.org/10.1016/j.sna.2022.113661
Received 10 August 2021; Received in revised form 13 October 2021; Accepted 2 June 2022
Available online 8 June 2022

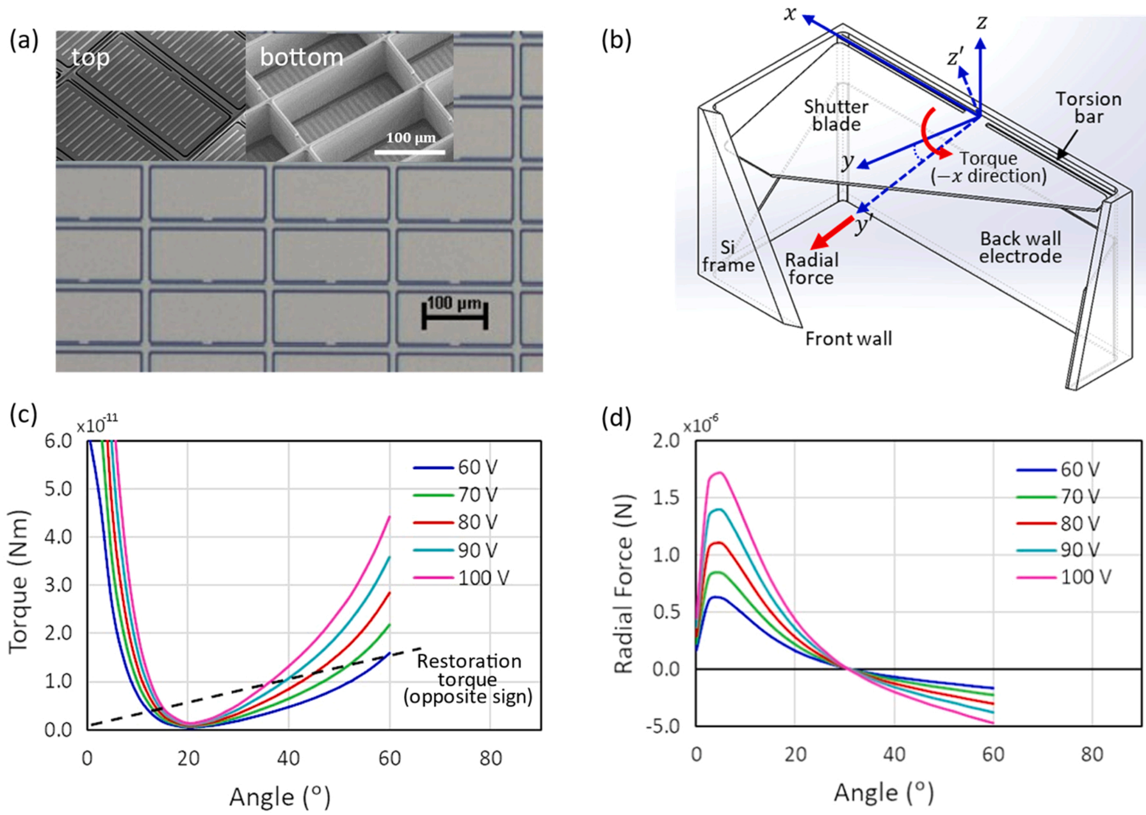

Fig. 1. Current NGMSA shutter design and its static electrostatic force profile. (a) Closeup of a fabricated NGMSA containing multiple microshutter units. Inset shows the SEM of a single shutter unit viewed from the top and bottom. (b) The schematic of a NGMSA unit shutter design with a back wall electrode. The positive torque and radial force direction with respect to the coordinate system are defined as shown. (c) and (d) show the torque profile and radial force of a shutter blade respectively under various positive blade electrode biases, V_{blade}, from 60V to 100V. Here, $V_{\mathrm{wall}} = V_{\mathrm{Si}} = 0$.

motion, rotating it far enough for the back electrode to capture it at a lower latching voltage [9]. Shutters with this design cannot be actuated in a quasi-static manner (without utilizing momentum), as attractive forces of the front wall prevent them from actuating past certain angles. [14].

In a recent study [15], the electrostatic force acting on the shutter blade is analyzed with a newly developed high-fidelity electrostatic finite element model. Fig. 1(c) and 1(d) show typical torque and radial force response to shutter blade angle position, θ, of the current NGMSA design when various blade electrode voltages are applied. There are two notable features on the electrostatic response. First, when $\theta = 15^{\circ}$ to $\theta = 25^{\circ}$, the torque is greatly reduced due to weak contribution of the electrostatic force normal to the shutter blade. Secondly, strong radial forces at small angles pull the blade towards the front wall, causing the torsion bar to stiffen and making actuation more difficult. The undesirable force will also increase the risk of shutters getting locked to the Si frame by asymmetric motion due to small geometry variations in the fabrication. To improve the electrostatic response of the legacy JWST MSA design, a modified keystone blade geometry with shorter blade length in the y-direction was proposed. The increased dynamic clearance

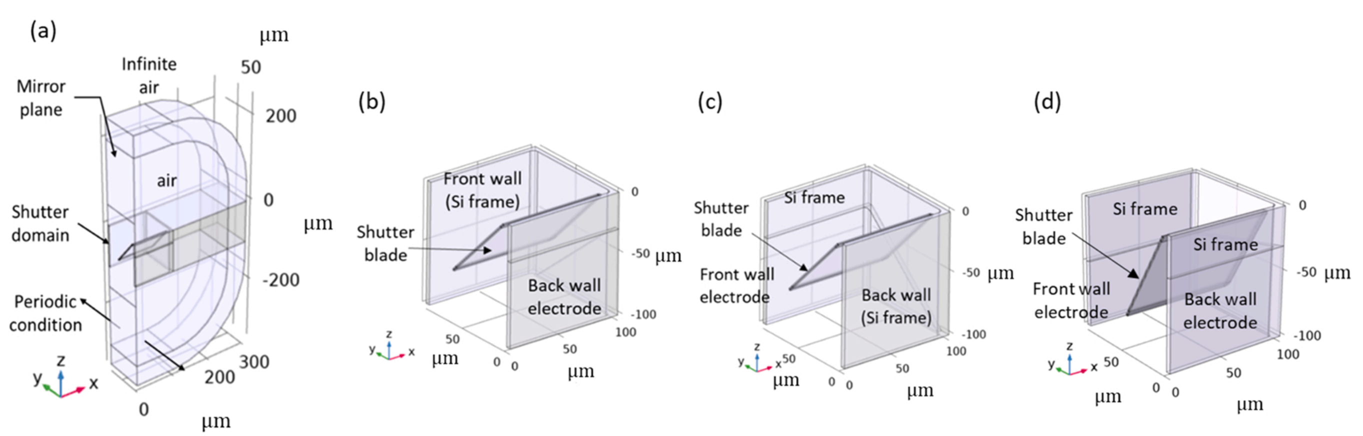

Fig. 2. Electrostatic model of the microshutter. (a) All half-shutter domains, the surrounding airfield domain, and an infinite air domain. (b) Zoomed-in view of the half-unit shutter with electrode on the back wall. (c) Zoomed-in view of the half-unit shutter with electrode on the front wall. (d) Zoomed-in view of the half-unit shutter with electrode on both the front and the back wall. The shutter blade is modeled as Al electrode at V_{blade}, the Si frame is grounded (0V), and the front and back wall electrodes are modeled as Al at $V_{\mathrm{wall}} = -30$V unless otherwise specified in the main text.

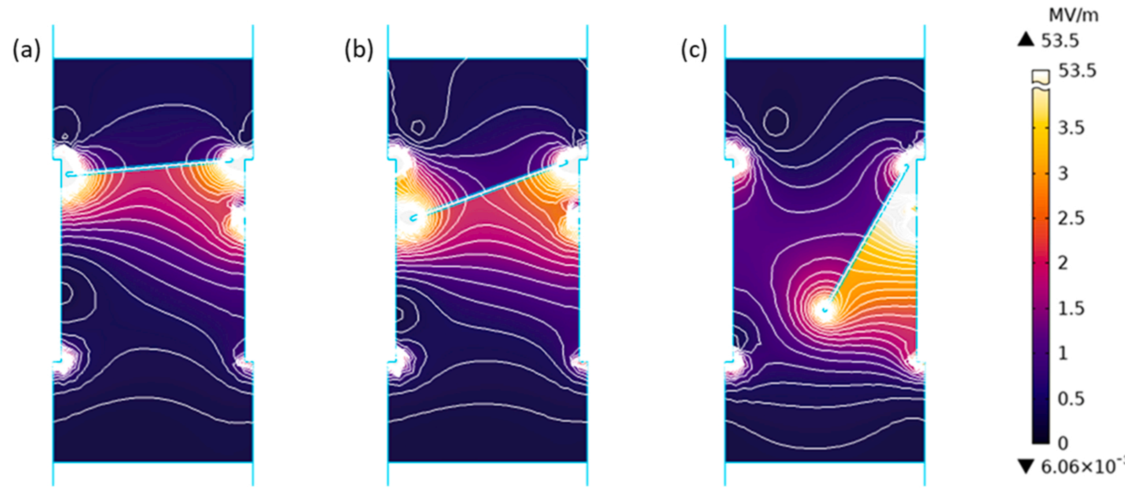

Fig. 3. Electric field surrounding the shutter blade in the *yz*-plane when the wall electrode is located on the back wall. The blade angle is at (a) 5°, (b) 20°, and (c) 60°, respectively. The applied voltages are $V_{\text{blade}} = 60\text{V}$, $V_{\text{wall}} = -30\text{V}$, and $V_{\text{Si}} = 0$.

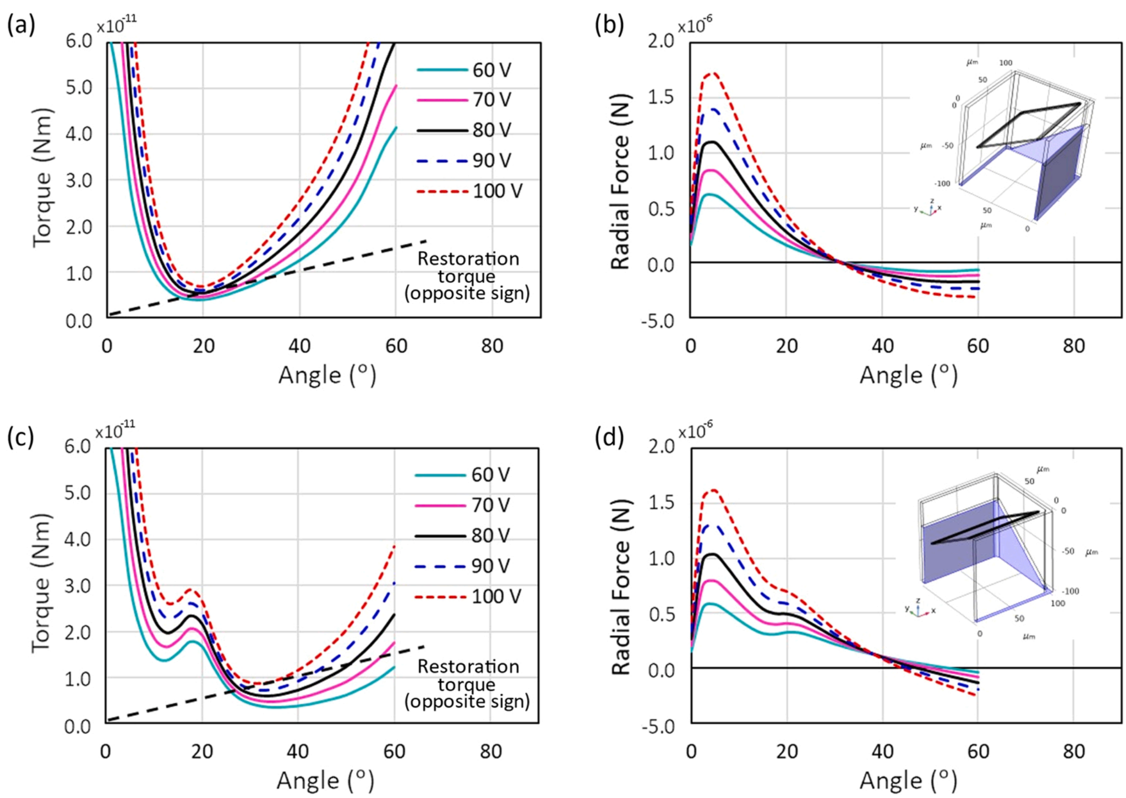

Fig. 4. Single wall electrode simulation results. (a) and (b) Electrostatic torque and radial force on the shutter as a function of V_{blade} and blade angle when the wall electrode is located on the back wall. (c) and (d) Electrostatic torque and radial force on the shutter as a function of V_{blade} and blade angle when the wall electrode is located on the front wall.

afforded by the new keystone blade geometry is expected to yield higher reliability in operation with a negligible decrease in fill factor. Devices utilizing the new findings of this study are currently being processed and are expected to be ready for testing in the near future.

In this paper, we investigate the effects of different wall electrode configurations. Electrostatic interaction between the shutter blade and the other electrode components are evaluated separately to understand their contribution to the actuation torque. The effects of Si frame and electrode are isolated to provide detailed understanding of the contribution of electrostatic forces from each shutter component. We find that the electrostatic actuation force can be understood in four stages: (1) the initial opening stage when θ is around 5°, most of the actuation force comes from the front wall of the Si frame which is closest to the blade edge; (2) the small-angle stage when θ is around 20°, the force can be modified with the existence of a front wall electrode; the front wall electrode provides strong downward electrostatic attraction on the shutter blade; (3) the mid-angle stage when θ is around 40°, the front wall electrode counteracts on the shutter opening, while the back wall electrode provides the main source of positive torque; (4) when $\theta > 60^{\circ}$, the shutter blade and back wall electrode distance closes and the electrostatic force increases rapidly, the blade quickly approaches the back

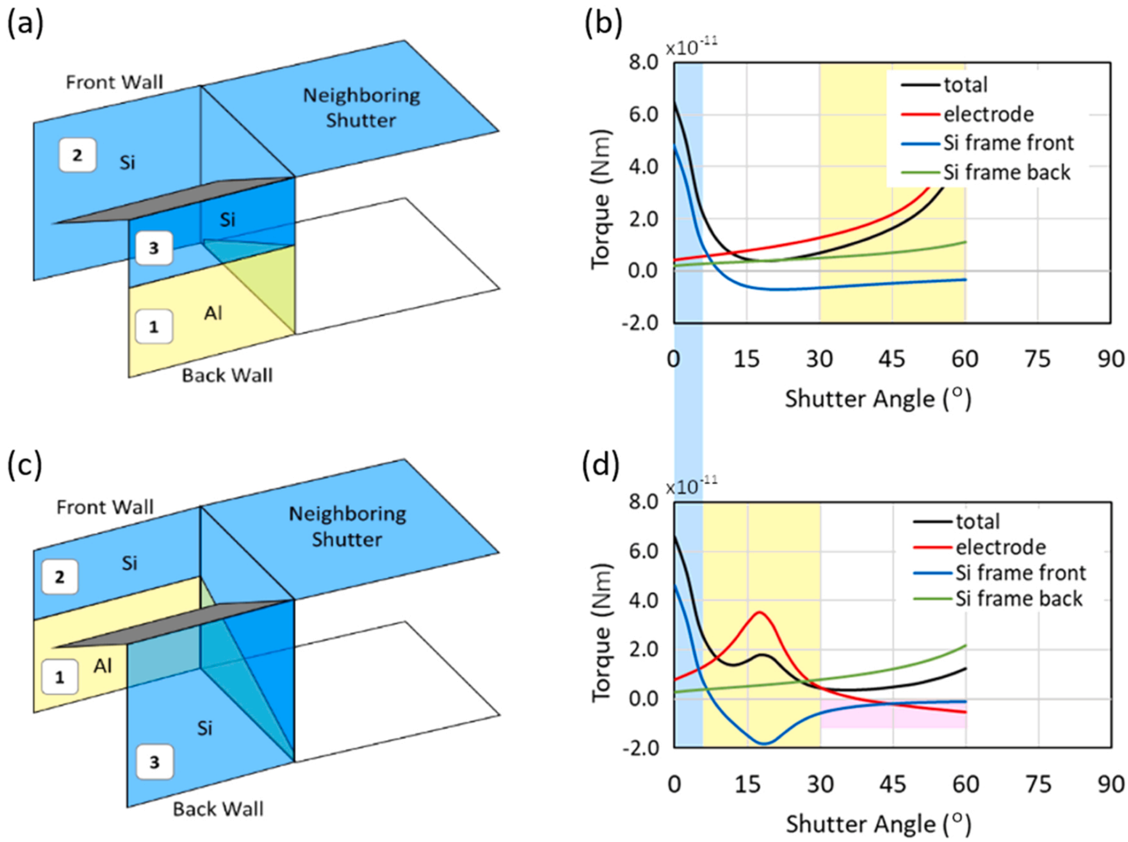

Fig. 5. Comparison of the isolated contributions from the electrode, front Si frame, and back Si frame of shutter systems. (a) Isolated regions for analysis with the wall electrode located on the back wall and (b) the resulting torque contribution from each region. (c) Isolated regions for analysis with the wall electrode located on the front wall and (d) the resulting torque contribution from each region. Region 1 (yellow) highlights blade angles when most of the electrostatic torque came from the front Si frame. Region 2 and 3 (blue) highlights blade angles when the electrode provides most torque. The red region highlights the counter torque caused by the front wall electrode at large angles that is not present with the back wall electrode design. (For interpretation of the references to colour in this figure legend, the reader is referred to the web version of this article.)

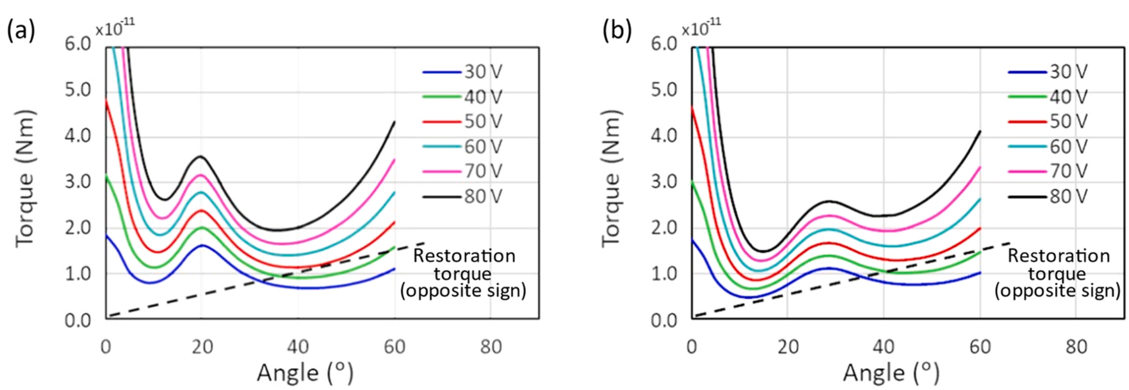

Fig. 6. Effect of electrode length on the bi-electrode design. (a) Torque on the blade as a function of V_{blade} and blade angle when the front and back electrodes are both 70μm long. (b) Torque on the blade as a function of V_{blade} and blade angle when the front and back electrodes are reduced to 60μm.

wall, and latching is guaranteed. Note that the torque profile between 0° and 60° (stages (1) to (3)) is the focus of the design optimization. The electrostatic response of the final design is presented in the full range (from 0° to 85°) at the end of this paper (Fig. 7(c) and 7(d)).

2. Method

A finite element model is used to simulate shutter devices with geometric designs of NGMSAs currently undergoing fabrication. As shown in Fig. 1(a), a single NGMSA shutter unit is a part of an array with 100μm × 200μm pitch. The unit shutter consists of an 84μm × 188μm shutter blade connected to a 2μm × 192μm torsion bar, a blade electrode covering the shutter blade surface, a Si frame support, and a back wall electrode, as shown in Fig. 1(b). The back wall electrode is 70 μm high, as shown in Fig. 2(b). The torsion bar acts as rotational hinge for the shutter blade, from 0° (fully closed) to 90° (fully opened). As shown in Fig. 2(a), the modeled shutter unit is assumed to be situated in an infinite array of shutters by applying period condition to the modeled half-shutter along the y-direction. Neighboring shutters in the ±*x*-directions are assumed inactive (closed), while shutters in the

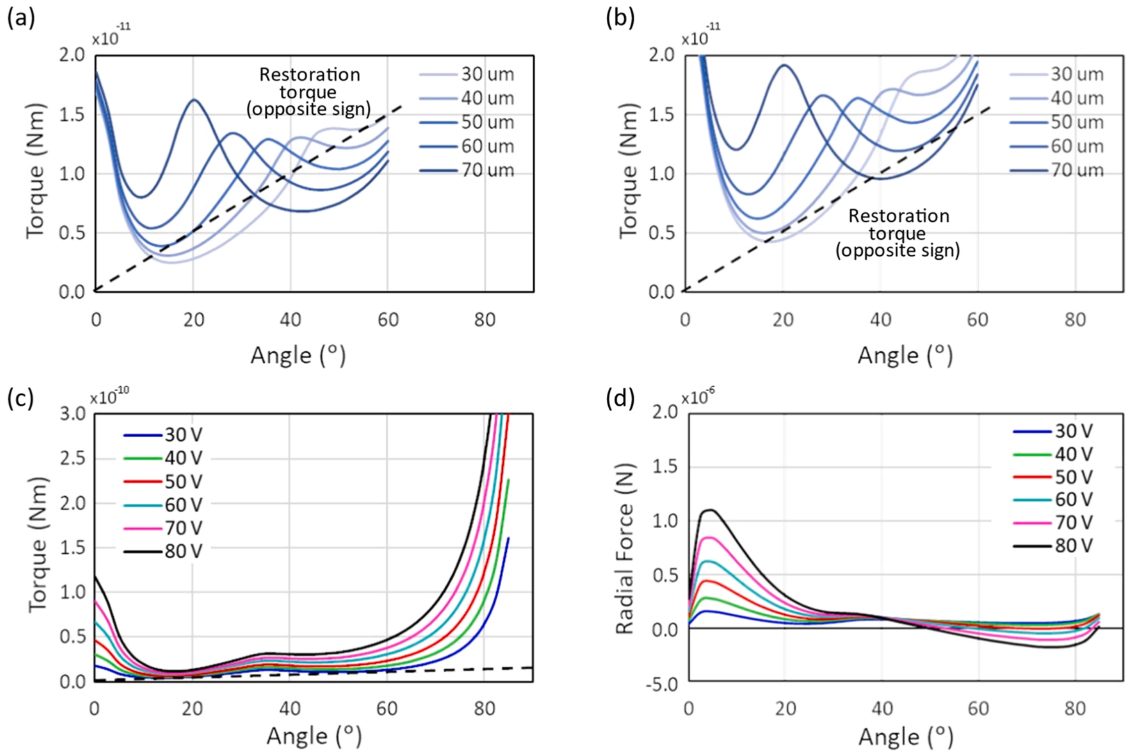

Fig. 7. Analysis of finding the optimal front wall electrode length while the back wall electrode is maintained at ***70 μm***. (a) Torque on the shutter blade with respect to front wall electrode length and blade angle when $V_{\text{blade}} = 30\text{V}$. (b) Torque on the shutter blade with respect to front wall electrode length and blade angle when $V_{\text{blade}} = 40\text{V}$. (c) Torque on the blade as a function of V_{blade} and blade angle and (d) radial force when the bi-electrode is designed optimally, with a 50μm front wall electrode and a 70μm back wall electrode.

$\pm y$-directions are actuated along with the unit shutter. Taking advantage of symmetry to simplify computation, only a half-unit shutter is modeled, and mirrored condition is applied to the yz-plane at $x = 0$. The shutter domain is surrounded by an air domain with the outer rim assumed to be infinitely far away and unaffected by the shutter electric field. Electrostatic effects on the thin torsion bar are assumed negligible and omitted from this model. Note that only pure rotation of the blade is considered in the model. As the deformation caused by the radial force is neglected, the resulting electrostatic torque and radial force are slightly underestimated especially at small angles. Details of the model have been described previously [15].

The electrode domain is either situated on the back wall (Fig. 2(b)), where it is placed in all implementations of our microshutters, the front wall (Fig. 2(c)), or both front and back walls (Fig. 2(d)). Triangular metal domains on the side walls are modelled to account for the sputtered metal during the angle deposition process used to fabricate the back wall electrode in all our microshutters. During simulation, a positive potential, V_{blade}, is assigned to the top surface of the blade. A negative potential, V_{wall}, is assigned to the wall electrode domain. The Si frame remains grounded at $V_{\text{Si}} = 0$. The effect of the electric field is statically calculated based on the rotational angle of the blade from 0° to 60°. Because of the large displacement and complexity of the electric field between non-parallel plates (Fig. 3), integration of the electrostatic forces along the field lines cannot be computed by analytical methods. Instead, finite element analysis is necessary to determine the non-linear electric field in the system.

The finite element simulation is conducted using the AC/DC module provided by COMSOL Multiphysics. Given the applied potential the electrostatic bundle solves the Gauss's law,

$$\nabla \cdot \boldsymbol{D} = \rho_v, \tag{1}$$

where $\boldsymbol{D}$ is the electric displacement and ρ_v is the charge density; and the Faraday Law,

$$\boldsymbol{E} = -\nabla V, \tag{2}$$

where $\boldsymbol{E}$ is the electric field and V is the applied potential. The force acting on the blade, $\boldsymbol{F}$, is calculated by Maxwell's stress tensor. Electrostatic forces acting on the surface of the blade domain are integrated,

$$\boldsymbol{F} = \int_{\partial\Omega} \boldsymbol{n} T \mathrm{d}S, \tag{3}$$

where $\boldsymbol{n}$ is the outward normal vector from the surface and T is the stress tensor. Radial force on the blade is defined as the parallel component of $\boldsymbol{F}$ to the blade surface pulling the blade in the y-direction. With the torsion bar acting as a hinge and rotation axis, we define the actuation torque, $\boldsymbol{\tau}_{\text{actation}}$, as the resultant torque from the total perpendicular force acting on the shutter blade:

$$\boldsymbol{\tau}_{\text{actuation}} = \int_{\partial\Omega} (r - r_o) \times (nT)\mathrm{d}S, \tag{4}$$

where $\boldsymbol{r}$ is the distance to the rotation axis.

The rotational stiffness, K, of the torsion bar was previously calculated by mechanical simulation based on measured silicon nitride properties [15]. In a torsion bar stiffness study that accounts for the plasticity of the aluminum conducting layer on top of the silicon nitride torsion bar, we find the difference in rotational stiffness with and without the additional aluminum layer is small. Therefore, the aluminum effect is omitted in this study. Then the restoration torque, $\boldsymbol{\tau}_1$, with respect to blade angle, θ, is approximated by the linear model,

$$\boldsymbol{\tau}_1(\theta) = K\theta. \tag{5}$$

For given V_{blade}, V_{wall}, and V_{Si}, the actuation torque, $\boldsymbol{\tau}_2$, must overcome the $\boldsymbol{\tau}_1$, that is,

$$\boldsymbol{\tau}_2 \quad (\theta) - K\theta > 0, \tag{6}$$

for the blade to open completely.

In the first part of the study, the effect of moving the location of the 70μm electrode from the current design on the back wall to the front wall is examined. Next, the Si frame and electrode parts of the shutter are considered separately in the simulation to determine the contribution each region has on the shutter blade. Finally, the optimal height of the electrode is determined for a bi-electrode design. In all cases, the Si frame is grounded at 0V, the wall electrode is held at -30V, and the voltage of the blade electrode is varied from 30V to 100V unless otherwise specified.

3. Results

3.1. Single wall electrode

The electrostatic response of the system is examined when the electrode is located either on the back wall or the front wall. Fig. 4(a) and 4(b) shows that, although higher voltages increase the overall torque exerted on the blade, the torque rapidly drops near 20° and confines blade movement below this angle if the vertical electrode is located on the back wall. With every 10V increase, the maximum radial force also increases by about 30%.

Moving the electrode to the front wall effectively shields the Si frame from acting on the electrode. Maximum radial force decreases by 60% just from relocation of the electrode, as shown in Fig. 4(d). The increased potential difference coming from the front wall allows the shutter to overcome the restoration torque beyond 25°, creating a bump in the torque profile in Fig. 4(c). However, electrostatic torque will drop below the restoration torque line beyond 30° and the shutter is once again confined.

To further understand how the electrode affects the radial force and electrostatic torque change throughout the actuation process, we isolate and analyze separate contributions from different electrode locations: the front Si frame, and the back Si frame, as shown in Fig. 5(a) and 5(c). Isolation is achieved by setting the region of interest to the voltage as in the full simulation while all other regions are set to floating electric conditions. A comparison of the results when $V_{\text{blade}} = 60$V for back wall electrode and front wall electrode designs are shown in Fig. 5(b) and 5(d). When actuation is initiated (blue region), the front Si frame contributes mostly to the actuation torque regardless of whether the electrode is located on the front or back wall. Around 10° to 20° (mid-range), contribution from the back wall components (either electrode or Si frame) is very small. The front Si frame generates torque counter to the opening direction, and the existence of a front wall electrode provides extra torque to compensate this effect. The back wall electrode only has a significant effect on the blade at large angles (greater than 30°). At this point, the blade has completely moved past the front wall. Electrostatic force from the front wall electrode becomes additional counter-torque on the blade. The most effective region for each electrode is highlighted yellow in Fig. 5(b) and 5(d).

Note that, since the goal is to understand the effect of the individual regions, contributions shown here are analyzed without accounting for the cross-interaction between the regions. In addition, contributions by the neighboring shutters and side wall regions are comparatively small, and no additional step was taken to decouple these regions for analysis. Therefore, the separate contributions (red, blue, and green lines) do not add up exactly to the total torque (black line).

3.2. Bi-electrode design

From the separate analysis, it is clear that there are advantages of having an electrode on the front wall as it eliminates the torque dip near $\theta = 20^{\circ}$ even when V_{blade} is as small as 30V. However, the merits for increased torque for smaller angles is diminished due to the increased counter-torque at large angles. Instead of removing the back wall electrode, using electrodes on both walls can overcome the shortcomings of either single electrode designs. With 70 μm electrodes on both walls, the back wall electrode will provide enough torque when the front wall electrode starts to counteract shutter rotation even when operated at $V_{\text{blade}} = 50$V (Fig. 6(a)). When $V_{\text{blade}} = 40$V, there is sufficient torque at small angles, but torque drops below restoration torque at mid-angles. To increase torque at this range, we may either decrease the front wall electrode length to reduce counter-torque, and/or increase back wall electrode length to increase forward torque. Fig. 6(b) shows that by decreasing electrode length on both walls to 60 μm, torque at mid angles increases marginally, although still insufficient for the shutters to operate at wall voltages lower than 50V.

A better configuration is to maintain the back wall electrode length as much as the fabrication method allows to maximize its torque contribution. From the isolated analysis discussed in the previous section, there is an optimal front wall electrode length such that counter-torque is minimized while still providing enough torque near 20° to overcome restoration torque. A length variation was done for the front wall electrode, with the back wall electrode maintained at 70μm.

First, the voltage is set to $V_{\text{blade}} = 30$V. As shown in Fig. 7(a), when the shutter is operated at $V_{\text{blade}} = 30$V, fine-tuning electrode length alone is not sufficient to obtain a torque profile that can overcome the restoration torque. Torque contributions from front wall electrodes that are shorter than 50μm are insufficient near 20°. Electrodes longer than 50μm generate too much counter-torque at large angles. Further reduction to actuation voltage will have to rely on design changes to other parts of the shutter. Instead, we fall back to modelling the shutter with $V_{\text{blade}} = 40$V. In this case, the shutter can be opened when the front wall electrode is between 40 μm to 60 μm long, as shown in Fig. 7(b). Taking the medium of the allowable length, the optimal bi-electrode design consists of a 50μm front wall electrode and a 70μm back wall electrode. Fig. 7(c) and 7(d) shows the electrostatic torque and radial force generated by this design under varying V_{blade}. The minimum V_{blade} that allows sufficient torque for actuation for this design is 40 V, bringing the totally voltage difference between the shutter blade and wall electrode ($V_{\text{wall}} = -30$V) to 70 V. Note that by lowering V_{blade} , the radial force can be significantly reduced, thus reducing the necessary clearance to avoid blade locking on the front wall.

4. Discussion

The bi-electrode design generates a strong downward electric field at the front edge of the blade when it is around the 15–20° angular range in which a torque dip is present when only the back wall electrode is used. Removing the torque dip makes it possible to actuate the shutters at lower blade-to-wall electrode voltage differences (around 70V) compared to shutter systems with only back wall electrodes (100V). Therefore, the requirements for the insulating layer between the electrode and frame can be lowered. This may simplify the fabrication processes in the future.

The counter torque of the front electrode at larger angles compensates some of the back wall torque increase after the blade overcomes the dip. This allows the electrostatic torque and restoration torque to be similar in magnitude when the blade is at angles less than 65°. A reduced V_{blade} requirement leads to significant reduction in blade acceleration. Although an acceleration of the shutter blade near 90° is inevitable, introducing a front wall electrode greatly reduces the blade-to-wall impact at latching and subsequently reduce the stress on shutter blade, torsion bar, and wall electrode metal and insulation. The shutter will open with a steadier velocity and shutter actuation will be more reliable and controllable.

The new configuration also lowers the radial force on the blade, which means the clearance gap between the shutter blade and Si frame can be reduced. This can be advantageous should a larger fill factor is required by a future mission.

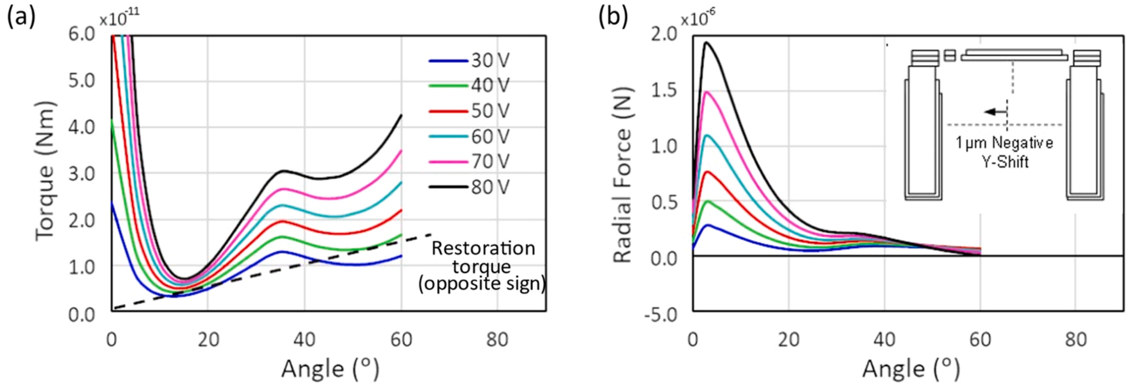

Fig. 8. Tolerance to alignment shift of shutters with bi-electrode design. (a) Torque on the blade as a function of V_{blade} and blade angle and (b) radial force of the optimized bi-electrode shutter system when the shutter and Si frame is subjected to a negative 1μm alignment shift as defined in the inset.

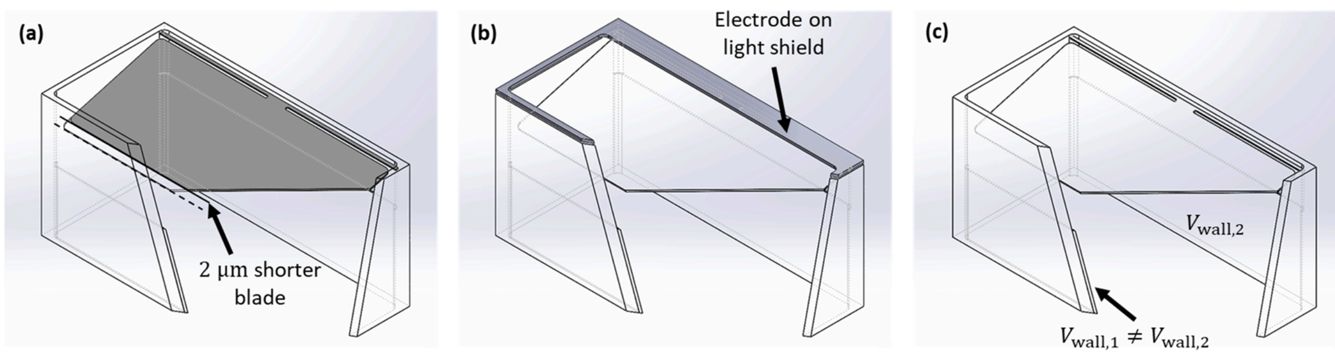

Fig. 9. Three possible enhancement schemes for the bi-electrode design. (a) shortening the blade by 2μm. (b) Adding an additional electrical control on the light shield above the blade. (c) Electrically separate front wall and back wall electrodes for additional voltage control.

Below we discuss the performance of the new design under the practical case when alignment variations are present. We also look at the effects of several possible enhancement schemes on improving the shutter's electrical response.

4.1. Effect of alignment variation

Due to the challenges of front-to-back alignment in the fabrication processes, alignment variations exist between the shutter blade and Si frame and are specified for the process. The shutter must maintain good

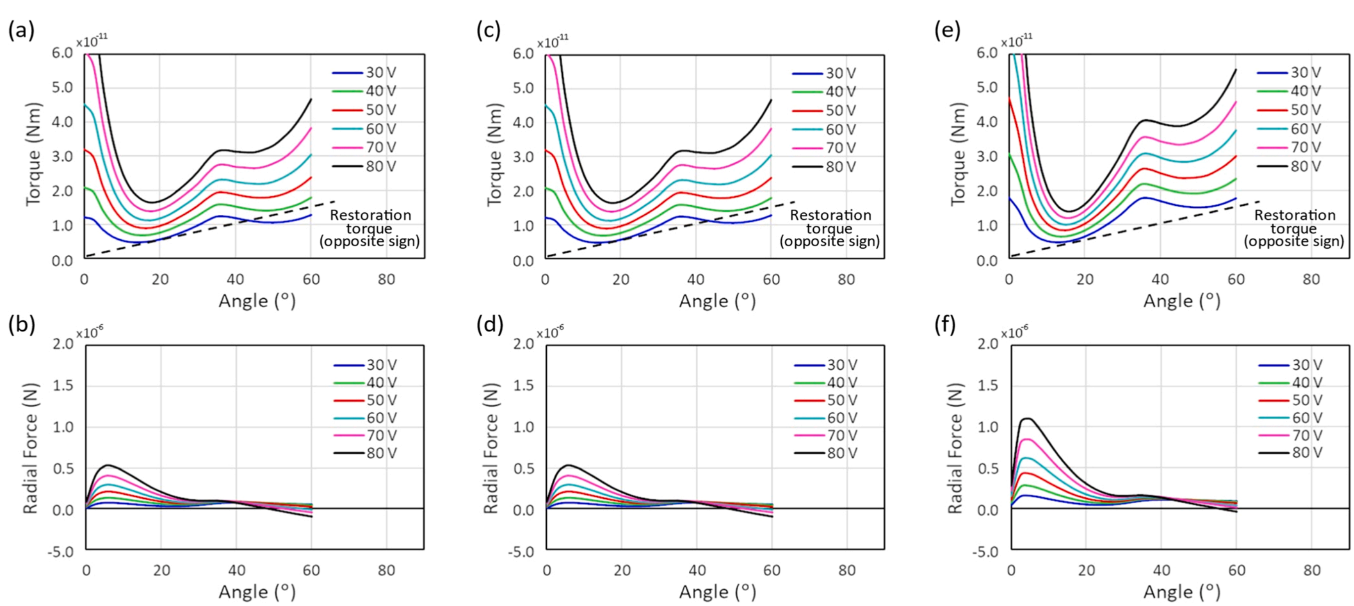

Fig. 10. Possible additional control of shutter response. (a) and (b) Torque and radial force response of a bi-electrode shutter system using a 2μm shorter shutter blade. (c) and (d) Torque and radial force response of a bi-electrode shutter system with an additional electrode located on top of the light shield. (e) and (f) Torque and radial force response of a shutter system with separately controllable front wall and back wall row electrode, front wall set to V_{blade}.

performance under these conditions. Our previous study showed that, while a positive *y*-direction shift improves shutter response, a negative 1μm *y*-direction shift between the shutter blade and Si frame (defined in the inset of Fig. 8(b)) will cause significant torque decrease and an increase in radial force in the current NGMSA design [15]. Here, we examine the effect of the same negative 1 μm shift on the optimized bi-electrode design. The results are shown in Fig. 8. Consistent with previous findings, there is a decrease in electrostatic torque at small angles. However, unlike the response of a back wall electrode only design, torque from the new design is still sufficient to overcome restoration torque with only slight increase in V_{blade}. Radial force increase in this case is also less than for the back wall electrode only design.

4.2. Additional design enhancement

As we have seen, by using the optimized bi-electrode design the necessary actuation voltage is significantly lowered. From Fig. 7(a), we notice that a shutter system with $V_{blade} = 30$V can almost generate sufficient torque to overcome the restoration torque. By making additional modifications to the design, and even changes to the operation schemes, shutter performance can be further enhanced. Here we discuss three possible enhancement schemes shown in Fig. 9: (1) shortening the shutter blade, (2) adding additional electrical control to the light shields, and (3) electrically separate front wall and back wall electrodes.

Blade shortening has already been explored in the previous paper [15]. A 2μm shorter blade reduces the voltage necessary for actuation from 100V to 90V and the chance of blade-to-frame locking at the cost of a slight reduction to the active area. Here, we apply the same 2 μm blade shortening to the bi-electrode design for analysis. Fig. 10(a) and 10(b) shows only a slight improvement on electrostatic torque to the bi-wall system with a 2μm shorter blade, and the radial force is significantly reduced.

Next, an additional electrode is added on the top surface of the light shield and the bias of this electrode is set to be equal to V_{blade}. As shown in Fig. 10(c) and 10(d), no significant improvement to actuation torque is observed. However, the additional electrode can shield the blade from pull-in by the Si frame, thus radial force is effectively reduced. In addition to the slight improvement, an electrode situated above the shutter blade can be used to ensure proper closure for inactive shutters with properly applied bias.

Finally, Fig. 10(e) and 10(f) shows an example of the response of the bi-electrode system with separately controlled electrodes. Here, the front wall electrode is maintained at V_{blade} to shield the blade from front wall effects while the back wall electrode pulls the shutter in at −30V. The optimal operating bias of such a design can be determined.

5. Conclusion

We have investigated the voltage-torque relations of microshutter blades of different designs. It is found that a bi-electrode design with properly selected height can allow reliable shutter actuation at a voltage difference of 70V ($V_{blade} = 40$V and $V_{wall} = -30$V). This is significantly lower than necessary to actuate shutters in the current configuration, thus providing the challenge to our processing team to implement such a layout in a viable production process.

CRediT authorship contribution statement

study conception and design: M. Ke, A.S. Kutyrev, C.A. Kotecki, K. Kim, M.A. Greenhouse, M-P. Chang, R. Fettig, R.P. Brekosky;acquisition of data: M. Ke, K. Kim;analysis and/or interpretation of data: M. Ke, K. Kim, M-P. Chang, R. Fettig;drafting the manuscript: M. Ke, K. Kim, M-P. Chang, R. Fettig;revising the manuscript critically for important intellectual content: M. Ke, A.S. Kutyrev, C.A. Kotecki, K. Kim, M.A. Greenhouse, M-P. Chang, R. Fettig, R.P. Brekosky, Y. Hu;All authors reviewed the results and approved the final version of the manuscript.

Declaration of Competing Interest

The authors declare that they have no known competing financial interests or personal relationships that could have appeared to influence the work reported in this paper.

Acknowledgements

We would like to thank our former project lead Mary Li for her helpful guidance and discussions. This work was made possible by NASA Goddard Space Flight Center's Pathways Intern Employment Program and Detector Systems Branch and was supported by NASA through the Strategic Astrophysics Technology (SAT) grant 600–18-7126-Scalable Microshutters Systems for UV Visible and Infrared Spectroscopy.

References

[1] D.E. Burns, L.H. Oh, M.J. Li, D.P. Kelly, A.S. Kutyrev, S.H. Moseley, 2-D electrostatic actuation of microshutter arrays, J. Micro Syst. 25 (2016) 101–107, https://doi.org/10.1109/JMEMS.2015.2498411.

[2] K. Mori, K. Misawa, S. Ihida, T. Takahashi, H. Fujita, H. Toshiyoshi, A MEMS electrostatic roll-up window shade array for house energy management system, IEEE Photonics Technol. Lett. 28 (2016) 593–596, https://doi.org/10.1109/LPT.2016.2514299.

[3] J.R. Karpinsky, R.L. Clark, J.A. Hammer, D.M. Brown, MEMS microshutter SLM for intensity modulation, in: I. Cindrich, S.H. Lee, R.L. Sutherland (Eds.), Diffractive Hologr. Technol. Syst. Spat. Light Modul. VI, 1999, pp. 254–259, https://doi.org/10.1117/12.349335.

[4] G. Perregaux, P. Weiss, B. Kloeck, I. Vuilliomenet, J.-P. Thiebaud, High-speed micro-electromechanical light modulation arrays, in: Proc. Int. Solid State Sensors Actuators Conf. (Transducers '97), IEEE, 1997, pp. 71–74, https://doi.org/10.1109/SENSOR.1997.613584.

[5] S. Gonseth, G. Perregaux, R. Frosio, J.P. Thiébaud, H. Vuillomenet, P. Debergh, C. Underbjerg, J.T. Ravnkilde, H. Henningsen, Arrays of addressable contactless optical microshutters, Microsyst. Technol. 11 (2005) 1171–1175, https://doi.org/10.1007/s00542-005-0583-8.

[6] K. Motohara, T. Takahashi, H. Toshiyoshi, M. Mita, N. Kobayashi, N. Kashikawa, Development of microshutter arrays for ground-based instruments, Proc. Instrum. Extrem. Large Telesc. (2005) 3–7. ⟨http://web.natur.cuni.cz/uhigug/kletetschka/motoharaELT2006.pdf⟩.

[7] M.J. Li, T. Adachi, C. Allen, S. Babu, S. Bajikar, M. Beamesderfer, R. Bradley, K. Denis, N. Costen, A. Ewin, D. Franz, L. Hess, R. Hu, K. Jackson, M. Jhabvala, D. Kelly, T. King, G. Kletetschka, A. Kutyrev, B. Lynch, T. Miller, H. Moseley, V. Mikula, B. Mott, L. Oh, J. Pontius, D. Rapchun, C. Ray, K. Ray, E. Schulte, S. Schwinger, P. Shu, R. Silverberg, W. Smith, S. Snodgrass, D. Sohl, L. Sparr, R. Steptoe-Jackson, V. Valeriano, L. Wang, Y. Zheng, C. Zincke, Complex MEMS device: microshutter array system for space applications, Micro Nanotechnol. Def. Secur 6556 (2007), 655602, https://doi.org/10.1117/12.721502.

[8] L.H. Oh, M.J. Li, K. Kim, A.S. Kutyrev, S.H. Moseley, N.P. Costen, G. Manos, D. P. Kelly, Fabrication and Sub-Assembly of Electrostatically Actuated Silicon Nitride Microshutter Arrays. 2018 Solid-State, Actuators, Microsystems Work. Tech. Dig., Transducer Research Foundation, San Diego, 2018, pp. 120–123, https://doi.org/10.31438/trf.hh2018.35.

[9] M.J. Li, E. Aguayo, R.P. Brekosky, D.E. Burns, A. Carter, M.P. Chang, N.P. Costen, R.K. Fettig, D.E. Franz, M.A. Greenhouse, G. Hu, K. Kim, D.P. Kelly, C.A. Kotecki, A. S. Kutyrev, S.R. McCandliss, T.M. Miller, S.H. Moseley, L. Oh, K. Ray, S. Rodriguez, F. Wang, B. Welch, Successful demonstration of an electrostatically actuated microshutter system for space telescope flight missions, J. Micro Syst. 29 (2020) 1079–1082, https://doi.org/10.1109/JMEMS.2020.3005585.

[10] X. Liu, T. Takahashi, M. Konishi, K. Motohara, H. Toshiyoshi, Random access addressing of MEMS electrostatic shutter array for multi-object astronomical spectroscopy, Micromachines 11 (2020), https://doi.org/10.3390/MI11080782.

[11] S.R. McCandliss, FORTIS Takes Flight on Mission to Analyse Comet ISON, (2013). ⟨https://physics-astronomy.jhu.edu/2013/11/27/fortis-takes-flight-on-mission-to-analyze-comet-ison/⟩.

[12] A. Hirsch, Johns Hopkins-Built Rocket Gets Brief Glimpse of a Galaxy Far, Far Away, (2015). ⟨https://hub.jhu.edu/2015/12/18/sounding-rocket-launch-observes-galaxy-far-far-away/⟩.

[13] M.D. Jhabvala, D. Franz, T. King, G. Kletetschka, A.S. Kutyrev, M.J. Li, S.E. Meyer, S.H. Moseley, S. Schwinger, R. Silverberg, Development and operation of the

microshutter array system, Micro Nanotechnol. Space, Def., Secur. Ii. 6959 (2008) 69590C, https://doi.org/10.1117/12.775768.
[14] M.P. Chang, R.P. Brekosky, A.D. Brown, N.P. Costen, M. Greenhouse, G. Hu, K. Kim, C.A. Kotecki, A.S. Kutyrev, M.J. Li, S.R. McCandliss, F.H. Wang, E. J. Aguayo, Development of the next generation microshutter arrays for space telescope applications, 15th IEEE Int. Conf. Nano/Micro Eng. Mol. Syst. NEMS 2020. (2020) 89–92, https://doi.org/10.1109/NEMS50311.2020.9265604.
[15] K. Kim, A.S. Kutyrev, M.J. Li, M.A. Greenhouse, Actuation force analysis and design optimization of microshutter array by numerical simulation method, Eng. Res. Express 3 (2021), 015007, https://doi.org/10.1088/2631-8695/abd41f.

Ming Ke is a PhD student in Mechanical Engineering at the University of California, Los Angeles. Her research focuses on 2D material transport properties and MEMS device applications. She joined the Detector Systems Branch at NASA Goddard Space Flight Center as a pathways intern in 2020 to support the development of next generation microshutters.

Dr. Alexander S. Kutyrev received his PhD. degree in astrophysics at the Moscow State University in Russia in 1986. His research interests span from zodiacal light to early type B stars, diffuse interstellar medium to studies of gamma-ray bursts and cosmology. All these scientific interests are closely related to experimental work on the instrumentation in optical and IR astronomical spectroscopy, in particular for spaceborne observatories, such as Spitzer, Swift, JWST and Roman Space Telescope. Dr. A. Kutyrev is currently a research associate at the University of Maryland, College Park, MD.

Carl Kotecki has been an electronics engineer at NASA GSFC for 34 years. His experience has been in the design, fabrication and testing of detectors, radiation hard high voltage CMOS, microfluidic devices, CNT & UNCD electron emitters and MEMS devices. He is currently the systems & lead testing engineer for the next generation microshutter arrays. He has served as the detector expert for the Instrument Design Lab in more than 85 studies and lead systems engineer for 15 studies. He is currently serving as the detectors source matter expert supporting the Astrophysics PCOS & COR program office.

Kyowon Kim is an Electrical Engineer at Science Systems & Applications Inc., working for Detector Systems Branch at NASA Goddard Space Flight Center. Kyowon specializes in design and testing of electrical and optical devices as well as processing. He has been working for Next Generation Microshutter Array project more than 5 years and he made several critical contributions including an effective actuation test system, driver electronics and operation codes, and an accurate electrostatic simulation model. He received the Ph.D. degree in Electrical Engineering from University of Maryland, College Park, MD, in 2015.

Matthew A. Greenhouse is an astrophysicist at NASA Goddard Space Flight Center. He is a Project Scientist for the James Webb Space Telescope Program and is Principle Investigator for NASA's Strategic Technology Development Project for Next Generation Micro-Shutters.

Meng-Ping Chang is a Product Development Lead in the Detector Systems Branch at NASA Goddard Space Flight Center. During his tenure with NASA he supported various ground and spaceborne projects including NG-MSA, ATHENA, HIRMES, CLASS, XRISM, XARM, PIPER, and HAWC+ . His research interests focus on miniaturization of sensors and actuators using MEMS, microfluidics, and nanotechnologies. He receives his PhD in mechanical engineering from the University of Michigan at Ann Arbor in 2008.

Rainer Fettig studied Physik at Karlsruhe University (Now Karlsruhe Institute of Technology - KIT) where he developed and built thermoelectric detectors for the CIRS Instrument on Cassini. After delivery he spent 6 years at NASA Goddard Space Flight Center developing different microstructures including microshutters. Returning to Germany in 2002 he briefly worked at KIT and started freelancing in 2004. Since then the is supporting various customers including ESA, NASA, ZEISS and Lusospace. He joined the Microshutter team again in 2020 as a technical Co-I.

Regis Brekosky is currently a Fabrication Team Lead for the Detector Systems Branch at NASA Goddard Space Flight Center where he designs and fabricates sensor arrays for space telescopes, sounding rocket experiments, balloon experiments, SOFIA and the Space Station. These arrays incorporate either ion implanted or Transition Edge Sensors (TES) technologies and are optimized for infrared or x-ray wavelengths. His past and present projects include COBE, AXAF, XQC, Constellation-X, ASTRO-E, ASTRO-E2, ASTRO-H, HAWC+ , PIPER, BETTII, μCIT, HIRMES, EHD, and NGMSA/FORTIS.

Yongjie Hu is an Associate Professor at the School of Engineering and Applied Science, University of California, Los Angeles. His group exploits interdisciplinary experimental and theoretical approaches to investigate energy transport mechanisms and device applications, with an emphasis on developing advanced materials and characterize nanoscale energy processes. He received his PhD degree from Harvard University and postdoctoral fellowship from Massachusetts Institute of Technology. His research has been recognized by diverse research societies through their awards including the Alfred P. Sloan Research Fellowship, ASME Bergles-Rohsenow Young Investigator Award, National Science Foundation's CAREER Award, and U.S. Air Force Young Investigator Award.